



**HAL**  
open science

## Comparative accuracy and resolution assessment of two prototype proton computed tomography scanners

G. Dedes, H. Drostén, S. Götz, J. Dickmann, C. Sarosiek, M. Pankuch, Nils Krah, Simon Rit, V. Bashkirov, R.W. Schulte, et al.

### ► To cite this version:

G. Dedes, H. Drostén, S. Götz, J. Dickmann, C. Sarosiek, et al.. Comparative accuracy and resolution assessment of two prototype proton computed tomography scanners. *Medical Physics*, In press, 10.1002/mp.15657 . hal-03637368v1

**HAL Id: hal-03637368**

**<https://hal.science/hal-03637368v1>**

Submitted on 11 Apr 2022 (v1), last revised 18 Jul 2022 (v2)

**HAL** is a multi-disciplinary open access archive for the deposit and dissemination of scientific research documents, whether they are published or not. The documents may come from teaching and research institutions in France or abroad, or from public or private research centers.

L'archive ouverte pluridisciplinaire **HAL**, est destinée au dépôt et à la diffusion de documents scientifiques de niveau recherche, publiés ou non, émanant des établissements d'enseignement et de recherche français ou étrangers, des laboratoires publics ou privés.

# Comparative accuracy and resolution assessment of two prototype proton computed tomography scanners

G. Dedes<sup>1,a</sup>, H. Drosten<sup>1</sup>, S. Götz<sup>1</sup>, J. Dickmann<sup>1</sup>, C. Sarosiek<sup>2</sup>, M. Pankuch<sup>3</sup>, N. Krah<sup>4</sup>, S. Rit<sup>4</sup>, V. Bashkurov<sup>5</sup>, R. Schulte<sup>5</sup>, R.P. Johnson<sup>6</sup>, K. Parodi<sup>1</sup>, E. DeJongh<sup>7</sup>, G. Landry<sup>8,9,1</sup>

<sup>1</sup> Department of Medical Physics, Faculty of Physics, Ludwig-Maximilians-Universität München, Am Coulombwall 1, 85748 Garching b. München, Germany

<sup>2</sup> Department of Physics, Northern Illinois University, 1425 W. Lincoln Highway, DeKalb, Illinois, United States of America

<sup>3</sup> Northwestern Medicine Chicago Proton Center, 4455 Weaver Parkway, Warrenville, Illinois, United States of America

<sup>4</sup> Univ Lyon, INSA-Lyon, Université Claude Bernard Lyon 1, UJM-Saint Etienne, CNRS, Inserm, CREATIS UMR 5220, U1294, F-69373, LYON, France

<sup>5</sup> Division of Biomedical Engineering Sciences, Loma Linda University, Loma Linda, CA 92354, United States of America

<sup>6</sup> Department of Physics, U.C. Santa Cruz, 1156 High Street, Santa Cruz, California, United States of America

<sup>7</sup> ProtonVDA LLC, 1700 Park Street STE 208, Naperville, Illinois, United States of America

<sup>8</sup> Department of Radiation Oncology, University Hospital, LMU Munich, 81377 Munich, Germany

<sup>9</sup> German Cancer Consortium (DKTK), 81377 Munich, Germany

<sup>a</sup> Authors to whom correspondence should be addressed. email: [g.dedes@lmu.de](mailto:g.dedes@lmu.de)

## Abstract

**Background:** Improving the accuracy of relative stopping power (RSP) in proton therapy may allow reducing range margins. Proton computed tomography (pCT) has been shown to provide state-of-the-art RSP accuracy estimation, and various scanner prototypes have recently been built. The different approaches used in scanner design are expected to impact spatial resolution and RSP accuracy.

**Purpose:** The goal of this study was to perform the first direct comparison, in terms of spatial resolution and RSP accuracy, of two pCT prototype scanners installed at the same facility and by using the same image reconstruction algorithm.

**Methods:** A phantom containing cylindrical inserts of known RSP was scanned at the phase-II pCT prototype of the U.S. pCT collaboration and at the commercially oriented ProtonVDA scanner. Following distance-driven binning filtered backprojection reconstruction, the radial edge spread function of high-density inserts was used to estimate the spatial resolution. RSP accuracy was evaluated by the mean absolute percent error (MAPE) over the inserts. No direct imaging dose estimation was possible, which prevented a comparison of the two scanners in terms of RSP noise.

**Results:** In terms of RSP accuracy, both scanners achieved the same MAPE of 0.72% when excluding the porous sinus insert from the evaluation. The ProtonVDA scanner reached a better overall MAPE when all inserts and the body of the phantom were

41 accounted for (0.81%), compared to the phase-II scanner (1.14%). The spatial resolu-  
42 tion with the phase-II scanner was found to be 0.61 lp/mm, while for the ProtonVDA  
43 scanner somewhat lower at 0.46 lp/mm.

44 **Conclusions:** The comparison between two prototype pCT scanners operated in the  
45 same clinical facility showed that they both fulfill the requirement of an RSP accuracy  
46 of about 1%. Their spatial resolution performance reflects the different design choices  
47 of either a scanner with full tracking capabilities (phase-II) or of a more compact  
48 tracker system which only provides the positions of protons but not their directions  
49 (ProtonVDA).  
50

51 *Keywords:* proton CT, image quality, design choices, RSP, spatial resolution

## 52 I. Introduction

53 Radiation therapy with external proton beams offers the potential for highly conformal  
54 dose distributions with the possibility of healthy tissue sparing. The point where protons  
55 stop in the patient is dependent on the stopping power of the tissue they traverse. This  
56 is commonly expressed as relative to water and denoted as relative stopping power (RSP).  
57 An accurate three dimensional (3D) patient RSP image in treatment position is needed for  
58 accurate proton dose calculation. Errors in the 3D patient RSP image will cause proton range  
59 prediction errors, thus introducing range uncertainties that entail the use of safety margins.<sup>1</sup>  
60 Currently, RSP images are obtained by converting x-ray linear attenuation coefficients,  
61 acquired with single energy x-ray computed tomography (CT) imaging. This is often based  
62 on a stoichiometric calibration<sup>2</sup> which leads to institution-specific margin recipes, e.g., 3.5%  
63 plus 1 mm at the Massachusetts General Hospital or similar recipes at other proton centers.<sup>1,3</sup>

64 Besides CT imaging for treatment planning, the use of volumetric image guidance for  
65 proton therapy is becoming well established.<sup>4</sup> Beyond patient positioning, there is a need  
66 for adaptive re-planning based on accurate RSP estimation in 3D, when the patient is in  
67 treatment position at isocenter, which allows reduced planning margins. The leading example  
68 for improved RSP estimation is dual-energy x-ray CT (DECT), which after undergoing  
69 extensive phantom<sup>5-14</sup> and animal tissue validation,<sup>15-19</sup> has seen clinical implementation  
70 for treatment planning,<sup>20-22</sup> and which is now appearing in treatment rooms, but requires  
71 the patient to be moved away from isocenter for verification.<sup>23</sup>

72 An alternative is to use the proton beam itself for imaging and to acquire a proton

---

73 CT (pCT) scan of the patient on the treatment table. While x-ray interactions are sparse,  
74 multiple Coulomb scattering (MCS) of protons means that straight-path approximations in  
75 the reconstruction algorithm lead to poor spatial resolution.<sup>24</sup> A curved path approximating  
76 the true proton path can be estimated from measurements of the location of each proton  
77 before and after the object, and can be refined with information about the direction of  
78 the proton, inferred from two locations separated by air or materials with a low scattering  
79 power. The RSP line integrals are evaluated along these curved paths,<sup>25</sup> and thus, a pCT  
80 scanner equipped with tracking modules and an energy detector allows use of proton tracking  
81 information in image reconstruction. pCT reconstruction algorithms account for curved  
82 paths, either using iterative reconstruction<sup>26–28</sup> or filtered-backprojection.<sup>29–31</sup>

83 Several prototype pCT scanners have been presented in the literature,<sup>32–38</sup> and an early  
84 simulation study suggested that pCT may provide competitive ideal RSP accuracy compared  
85 to DECT.<sup>39</sup> Many of these scanners have been used to image phantoms, and experimental  
86 RSP accuracy is reported better than 1.6%,<sup>37</sup> 1.4%,<sup>40</sup> or 0.74%,<sup>38</sup> and was shown to be  
87 equivalent to state-of-the-art DECT in a comparison using known RSP tissue mimicking  
88 phantoms<sup>41</sup> with a mean absolute percentage error (MAPE) of 0.6%. Since various proton  
89 tracking pCT prototypes are in the early development stage, it is yet unclear what the  
90 optimal system design is. Two of the most advanced scanners currently in operation are the  
91 pCT collaboration’s phase-II scanner<sup>35</sup> and the commercially-oriented ProtonVDA (pVDA)  
92 scanner.<sup>42–44</sup> The phase-II scanner features silicon-strip tracking modules registering both  
93 the location and direction of protons before and after the object, and a five-stage energy  
94 detector. The pVDA scanner uses scintillating fibers tracking modules which register only  
95 position with initial direction vectors derived from the beam geometry, and a single stage  
96 energy detector requiring variation of the proton beam energy. Given the differences in  
97 particle tracking and energy detection between the scanners, and since they are both available  
98 at the Northwestern Medicine Chicago Proton Center, this study aimed at performing the  
99 first comparison of two particle tracking pCT scanner prototypes.

## 100 II. Materials & methods

101 To compare the performance of the new commercial pVDA system against the well-studied  
102 phase-II scanner in terms of spatial resolution and RSP accuracy, we scanned a phantom of

---

103 known RSP with both systems. In order to focus on the hardware differences between the  
 104 two scanners, preconditioning of the data before image reconstruction and the reconstruction  
 105 algorithm were the same for both scanners. Details about the scanners, the data processing,  
 106 the reconstruction algorithm and the scanned object are given in the subsequent sections.

## 107 II.A. Phase-II prototype scanner

108 The phase-II scanner<sup>34</sup> is depicted in figure 1, left panel, and was designed by the pCT  
 109 collaboration (at the Baylor University, Loma Linda University, and the University of Cali-  
 110 fornia at Santa Cruz). The particle tracking system consists of two tracking modules,<sup>35</sup> one  
 111 before and one after the object, measuring position and direction information, as well as a  
 112 scintillating detector<sup>45</sup> measuring the residual energy.

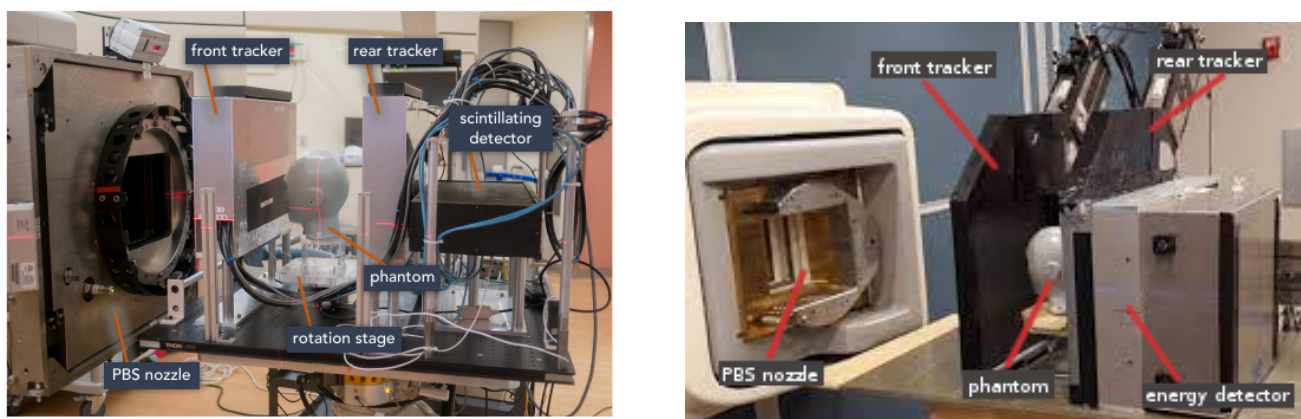


Figure 1: (Left) phase-II scanner with various parts of the system indicated (taken from<sup>46</sup> - © Institute of Physics and Engineering in Medicine. Reproduced by permission of IOP Publishing. All rights reserved). (Right) Photo of the pVDA scanner with its main parts labeled.

113 Each of the two tracking modules<sup>35</sup> consists of two tracking planes separated by 50 mm,  
 114 each measuring the coordinates of every incoming proton. Using the two position measure-  
 115 ments and the direction vector, the most likely path (MLP) can be estimated.<sup>25</sup> Coordinates  
 116 are determined as hit locations of two adjacent planes of single-sided silicon strip detectors  
 117 with lateral and vertical strip orientation, respectively, to provide two-dimensional coordi-  
 118 nate measurements. Laterally, each tracking plane consists of four modules that are glued

119 together, resulting in an insensitive gap of 0.6 mm.

120 The energy detector<sup>45</sup> consists of five longitudinal segments of UPS-923A<sup>47</sup>  
121 (RSP = 1.038) which are individually wrapped in reflective material and coupled to a  
122 photo-multiplier. Each segment is referred to as a *stage* and their longitudinal depth is  
123 51 mm. Each incident proton can produce up to five readings in the analog-digital convert-  
124 ers (ADCs) of the photo-multipliers. The segmented design with five stages was chosen to  
125 minimize water-equivalent path length (WEPL) noise and to make it almost independent  
126 of the scanned object.

127 The scanner has been shown to produce a near 100 % detection efficiency for count rates  
128 up to 1 MHz with homogeneous proton fluence.<sup>35</sup> For operation of the scanner with scanned  
129 pencil beams, the local count rate increases and a pileup-free operation was demonstrated  
130 for count rates up to 400 kHz.<sup>46,48</sup> For the purpose of this study, a 200 MeV broad proton  
131 beam was utilized with the phase-II scanner. More details about the beam characteristics  
132 are given in section II.F.

## 133 II.B. pVDA scanner

134 The second pCT scanner under investigation is the prototype<sup>43</sup> of ProtonVDA LLC  
135 (Naperville, Illinois, USA) depicted in figure 1, right panel. Its more compact design is  
136 intended for future clinical use. The system has two tracking modules, one upstream and  
137 one downstream the scanned object. Unlike the phase-II scanner, these tracking modules  
138 only consist of a single tracking plane and no direction information is acquired directly.

139 Tracking is realized through scintillating fibers. Each tracking module consists of two  
140 layers of fibers, one oriented horizontally and one vertically to provide two-dimensional  
141 coordinate measurements. The system can only be operated with scanned pencil beams due  
142 to the multiplexing of the tracking fibers: multiple non-adjacent fibers are connected to one  
143 of many photomultipliers and an exact and unambiguous location is determined using the  
144 approximate location of the pencil beam.

145 The energy detector is realized as a 130 mm thick monolithic scintillator block. The  
146 scintillation light is measured by 16 individual photomultipliers, which are distributed lat-  
147 erally across the surface of the detector. Due to the limited depth of the sensor, only thin

148 objects can be scanned with a single proton energy. To scan thicker objects, scans of several  
149 incident proton energies are combined, rejecting protons that stopped in the object or com-  
150 pletely penetrated the scintillator. The system is designed for count rates of up to 10 MHz;<sup>43</sup>  
151 in this experiment, it was operated reliably at count rates of 1 – 2 MHz.

## 152 II.C. Data processing of the phase-II scanner

153 The data processing steps of the phase-II scanner, before data conditioning for reconstruction  
154 and image reconstruction itself, have been described Schultze et al.<sup>49</sup> The acquired data from  
155 the tracking detector and the energy detector are converted to coordinates in the reference  
156 system of the trackers and WEPL values for proton histories that are not rejected for various  
157 reasons, e.g., incomplete tracking data or suspected pileup events.

158 To generate WEPL measurements from the ADC readout, the phase-II scanner makes  
159 use of an elaborate calibration procedure based on data from a double-wedged polystyrene  
160 phantom (RSP= 1.03) complemented by one to four rectangular polystyrene blocks.<sup>50</sup> A  
161 detailed description of the calibration procedure is given in several previous publications,  
162 including Bashkirov et al.<sup>45</sup>, Piersimoni et al.<sup>50</sup>, Dedes et al.<sup>51</sup> and Schultze et al.<sup>49</sup>

163 The calibration runs cover the complete WEPL range of the detector. They are used to  
164 establish two-dimensional histograms binned by WEPL and energy deposit to the stopping  
165 stage. The stopping stage is defined as the furthest stage where the energy deposit ex-  
166 ceeded a certain threshold (usually 1 MeV) and the WEPL can be inferred from the tracking  
167 information and the geometry of the calibration phantom. From this histogram, for each  
168 energy deposit, the most frequent WEPL is found, which allows establishing an energy-to-  
169 WEPL calibration curve for each of the five stages of the energy detector. These calibration  
170 curves are then applied to subsequent imaging runs to convert the ADC measurements of  
171 an unknown object to WEPL values. Finally, the WEPL values are combined with the  
172 four coordinate measurements in the tracker and yield the proton-by-proton WEPL, up-  
173 stream/downstream position, and upstream/downstream direction information used in the  
174 reconstruction algorithm, as described by Schultze et al.<sup>49</sup>.

175 During this particular experiment, noise on the energy detector data was slightly ele-  
176 vated compared to past scans. This effect was manifested as increased RSP artifacts com-

pared to what was previously observed<sup>41</sup> for the energy threshold of 1 MeV to select the stopping stage. To reduce the ring artifacts which intersect the inserts and affect the RSP accuracy, the stage threshold was varied from 1.5 MeV to 3 MeV in 0.25 MeV steps, in addition to the default threshold value. The optimal threshold value was found to be 1.5 MeV, yielding images with ring artifacts of comparable amplitude to what was previously reported in published literature.<sup>41</sup>

## II.D. Data processing of the pVDA scanner

The pVDA scanner is calibrated without the use of a dedicated phantom and instead utilizes multiple acquisitions at different incident beam energies. The calibration procedure converts the photomultiplier signals to residual proton range in WEPL. Protons are delivered at 44 energies ranging from 100.8 to 164.7 MeV, with their range reduced by a 6.5 cm water-equivalent material uniform absorber, covering proton ranges between 1.25 and 12 cm. 1.25 cm is roughly the minimum proton range needed to traverse the preceding detector material, enter the scintillator and produce a signal just above the noise threshold. Each incident energy smaller than the maximum energy corresponds to a reduction in range and produces energy deposits approximately proportional to the equivalent WEPL in the energy detector. Via this calibration procedure, for each of the 44 proton beam energies, the corresponding WEPL in the detector is mapped to the ADC number produced by the detector. The exact procedure, including the correction of the spatial dependence of the signal with respect to the locations of the energy deposit and the photomultiplier, is described in detail in DeJongh *et al.*<sup>43</sup>

Since the system's energy detector is too thin to cover the desired WEPL range directly, data from multiple energies are merged. The calibration needs to be performed only once, since calibrated WEPLs can be shifted by the difference in range of a lower incident energy. For the imaging runs presented in this work, three incident energies (118 MeV, 160 MeV and 187 MeV) were acquired throughout the field of view, which resulted in an increased imaging dose, but could be avoided in case prior knowledge of the scanned object is available.<sup>52</sup> Each of the beam energies covered a specific WEPL range in the object scanned in this experiment, with some overlapping WEPLs between them, as indicated in table 1. The first overlap region extends from approximately 50 mm to about 90 mm and is covered by the 118 MeV



207 and the 160 MeV beams, respectively. The second overlap region spans 100 mm to 125 mm  
 208 and was sampled by the 160 MeV and the 187 MeV beams. For that particular dataset,  
 209 it was found that using protons from the 187 MeV beam together with protons from the  
 210 other beams for sampling the same WEPL regions caused considerable ring-shaped image  
 211 artifacts. Therefore, the use of the 187 MeV was reduced to the bare minimum, namely  
 212 for WEPLs larger than 125 mm. With this filtration the number of protons available for  
 213 reconstruction was reduced by 38% compared to the initial dataset.

214 The proton angle at the front tracker is determined from the location of the proton  
 215 hit and the distance from the steering magnets in the beamline.<sup>43</sup> The rear tracker angle is  
 216 determined by a MLP calculation. During that procedure, the most likely combination of  
 217 exit position from the object and exit angle, given the upstream tracker position, upstream  
 218 angle, and downstream tracker position, is estimated on a proton-by-proton basis.

Table 1: WEPL sampling for the pVDA scanner. The first column indicates the energies used. The second column lists the WEPL interval covered by each energy. The third column shows the WEPL range finally used for reconstruction, after removing the overlap between the two higher energies.

Energy (MeV)	WEPL (mm)	WEPL for reconstruction (mm)
118	0 - 90	0 - 90
160	50 - 125	50 - 125
187	100 - 200	125 - 200

## 219 II.E. Phantom

220 The analyses performed in this work were based on scans of a custom-built phantom with  
 221 known RSP and geometry shown in figure 2. The phantom's body consists of blue wax with  
 222 an RSP of 0.980. It is 40 mm thick and has a diameter of 180 mm. It contains eight inserts  
 223 made of tissue-equivalent plastic materials, each with a diameter of 18 mm and with thickness  
 224 of 40 mm, listed in figure 2. The reference RSP ( $\text{RSP}_{\text{ref}}$ ) of each insert was determined in  
 225 another study<sup>42</sup> using a multi-layer ionization chamber.

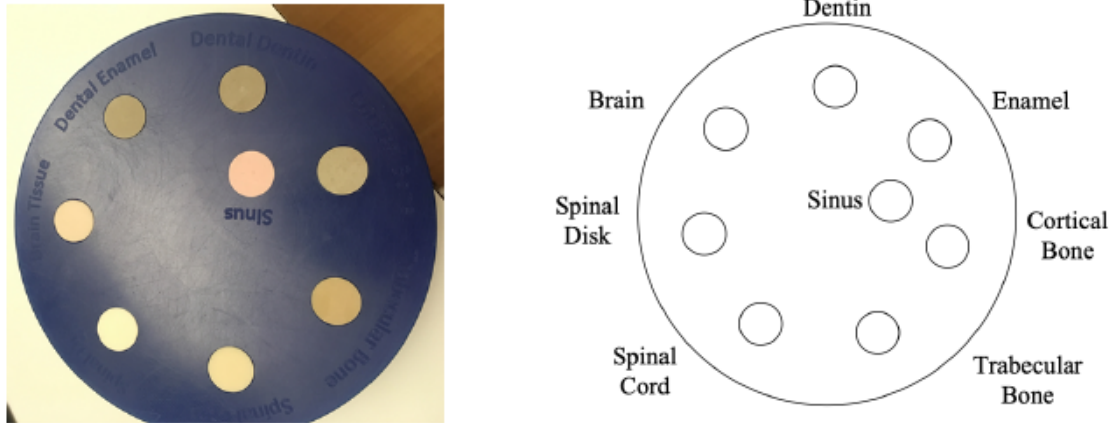


Figure 2: (Left) Photo of the cylindrical phantom made of plastic body and containing eight plastic tissue equivalent inserts. (Right) Drawing of the phantom with the inserts labeled. It should be noted that the labels of the enamel and dentin inserts as seen in the photograph have been mistakenly swapped in the manufacturing process. The correct positions are shown in the drawing.

## 226 II.F. Datasets

227 The phase-II scanner data of the cylindrical phantom were acquired at the Northwestern  
 228 Medicine Chicago Proton center using a 200 MeV wobbled beam of approximately 1.7 cm  
 229 size ( $1\sigma$  at isocenter). The acquisition was obtained in a continuous rotation mode, which  
 230 means that the phantom was rotating throughout the beam-on time and the data were later  
 231 on split into 360 projections, each one covering an arc of  $1^\circ$ , using the timestamp of each  
 232 proton and the known rotation speed (1 rpm) of the stage. The scan time was approximately  
 233 5 min, during which about  $3.6 \times 10^8$  protons were acquired at a 1 MHz rate. From the 360  
 234 projections, 90 projections at  $4^\circ$  steps were kept and used in the reconstruction. This choice  
 235 was made in order to have the same number of projections and at the same angular steps as in  
 236 the pVDA dataset, which was acquired in a step-and-shoot mode. The data were processed  
 237 with a calibration curve obtained on the same day with the same beam characteristics as the  
 238 imaging run. After cuts, in the processing of the raw data, the mean proton fluence in the  
 239 object was 30 protons/mm<sup>2</sup> per projection. As described in section II.C., the energy detector  
 240 stage threshold was optimized to suppress image artifacts. Prior to reconstruction, the data  
 241 were binned in  $2 \text{ mm} \times 2 \text{ mm}$  sized-pixels at the front tracker and  $3\text{-}\sigma$  cuts were applied on  
 242 the angle and WEPL distribution in each pixel.

243 The pVDA scanner data of the same phantom were acquired in the same facility in a

244 step-and-shoot mode (90 projections at  $4^\circ$  angular steps), by scanning a 0.4 – 0.8 cm size  
245 (energy dependent and quantified as  $1\sigma$  at isocenter) pencil beam over an area large enough to  
246 cover the phantom. Three incident energies (118 MeV, 160 MeV and 187 MeV) were utilized  
247 to sample the WEPL range of the phantom taking into account the limited thickness of the  
248 energy detector. The beam-on time, considering all three energies, was approximately 90 sec,  
249 during which about  $10^8$  protons were acquired at a rate between 1 and 2 MHz. This does not  
250 account for the overhead time for rotating the phantom between two projections (phantom  
251 rotation has been automated after that experiment). Additionally, about 10-20 sec were  
252 needed for beam energy switching. The three incident energies combined covered a WEPL  
253 range from 0 to approximately 200 mm (as shown in table 1). To avoid inadequate WEPL  
254 sampling, the WEPL interval covered by each energy overlaps with that covered by another  
255 energy. The extent of this overlap was tuned to provide the best possible image quality,  
256 as previously described in section II.D.. After the initial processing and merging, a mean  
257 fluence in the object of approximately 20 protons/mm<sup>2</sup> per projection were forwarded to  
258 the reconstruction. Similarly to the procedure followed for the phase-II scanner, prior to  
259 reconstruction, the data were binned in  $2\text{ mm} \times 2\text{ mm}$  sized-pixels at the front tracker and  
260  $3\text{-}\sigma$  cuts were applied on their angular and WEPL distribution in each pixel.

## 261 II.G. Reconstruction algorithm

262 Following the processing of the raw scanner data and the filtering on angle and WEPL, the  
263 volumetric RSP images were reconstructed using a dedicated filtered backprojection algo-  
264 rithm. A detailed description of the concept of the algorithm is given in Rit et al.<sup>29</sup> To  
265 account for the curved proton trajectories due to MCS, the path of every proton is esti-  
266 mated by an MLP formulation.<sup>25</sup> The MLP estimate is based on the position and direction  
267 information from the tracker in the case of the phase-II scanner, and on the positions from  
268 the tracker and the angles deduced in the processing of the data in the case of the pVDA  
269 scanner.

270 The proton-by-proton data were binned in projection images with  $1\text{ mm} \times 1\text{ mm}$  pixels for  
271 use with the RSP accuracy analysis and with  $0.2\text{ mm} \times 0.2\text{ mm}$  pixels in the case of the spatial  
272 resolution determination. The projections were then filtered and backprojected. In the last  
273 step, the pCT images were reconstructed as RSP maps in a grid of  $1\text{ mm} \times 1\text{ mm} \times 1\text{ mm}$

274 for RSP analysis or  $0.2 \text{ mm} \times 0.2 \text{ mm} \times 1 \text{ mm}$  for spatial resolution. The reconstruction was  
 275 applied to both scanner datasets without change of parameters.

## 276 II.H. RSP accuracy and spatial resolution

277 The RSP accuracy (percent RSP error) was quantified separately in each insert. A cir-  
 278 cular region-of-interest (ROI) with a radius of 7 mm (80% of the insert radius to avoid  
 279 insert boundaries) was applied around the insert centers and the mean reconstructed RSP  
 280 ( $\text{RSP}_{\text{mean}}$ ) in each ROI was calculated. The RSP accuracy ( $\text{RSP}_{\text{acc}}$ ) was then defined as:

$$281 \quad \text{RSP}_{\text{acc}} = \frac{\text{RSP}_{\text{mean}} - \text{RSP}_{\text{ref}}}{\text{RSP}_{\text{ref}}} \cdot 100\%, \quad (1)$$

282 where  $\text{RSP}_{\text{ref}}$  denotes the reference RSP of each insert. The uncertainty of the  $\text{RSP}_{\text{acc}}$   
 283 per insert is derived from the uncertainty on the  $\text{RSP}_{\text{ref}}$  and from the uncertainty on the  
 284  $\text{RSP}_{\text{mean}}$ , making use of error propagation. The former was defined as the uncertainty from  
 285 a 0.1 mm error in the sample thickness estimation during the multi-layer ionization chamber  
 286 measurement. The latter was based on the standard error of the mean (SEM), calculated  
 287 over the values of  $N$  voxels in the ROI:

$$288 \quad \text{SEM} = \frac{\sigma_{\text{rec}}}{\sqrt{N}}, \quad (2)$$

289 where  $\sigma_{\text{rec}}$  is the standard deviation of the reconstructed RSP values of the  $N$  voxels in the  
 290 ROI.

291 In addition to the RSP for each insert, the MAPE achieved for each scanner for that  
 292 particular phantom was also calculated as:

$$293 \quad \text{MAPE} = \frac{\sum_{i=1}^n |\text{RSP}_{\text{acc},i}|}{n}, \quad (3)$$

294 where  $n$  is the total number of inserts and  $\text{RSP}_{\text{acc},i}$  is the percent error for every insert  $i$   
 295 as calculated from equation 1. The uncertainty on the MAPE was calculated via an error  
 296 propagation based on the individual insert accuracy.

297 The spatial resolution was evaluated by calculating the modulation transfer function  
 298 (MTF) from the radial edge-spread function (ESF)<sup>53</sup> of the three inserts with the highest  
 299 RSP (enamel, cortical bone and dentin). After taking the average of 20 slices to reduce noise  
 300 in the images and determining the insert centers using a threshold followed by a center of  
 301 mass calculation, we followed the approach of Krah et al.<sup>54</sup> and Khellaf et al.<sup>31</sup> and modelled  
 302 the ESF as an error function with parameters  $A$ ,  $\mu$ ,  $\sigma$  and  $C$ .

$$303 \quad \text{ESF} = A \cdot \frac{1}{2} \left[ 1 + \text{erf} \left( \frac{r - \mu}{\sqrt{2}\sigma} \right) \right] + C, \quad (4)$$

304 where  $r$  is the distance of the sampled points to the insert center. Using the parameters  
 305 obtained by the fit of the ESF to the inserts, the frequency of the MTF at the 10% level,  
 306 used here as the metric for spatial resolution, is then given by:

$$307 \quad f_{\text{MTF}_{10\%}} = \sqrt{\frac{\ln 10}{2}} \cdot \frac{1}{\pi\sigma}. \quad (5)$$

308 The uncertainty on the  $f_{\text{MTF}_{10\%}}$  is estimated by propagating the uncertainty on  $\sigma$  from the  
 309 fit described in equation 4 to equation 5.

### 310 III. Results

#### 311 III.A. RSP accuracy and spatial resolution

312 For the comparison of the performance of the two scanners, the  $\text{RSP}_{\text{acc}}$  and spatial resolution  
 313 evaluations were applied on the pCT images (figure 3(a) for phase-II and figure 3(b) for  
 314 pVDA scanners, respectively). Ring-shaped artifacts are present in both images and to  
 315 some extent, affect the quantified  $\text{RSP}_{\text{acc}}$ . The difference image in figure 3(c) shows that  
 316 artifacts did not appear at the same location in both images. A slight residual misalignment  
 317 is the cause of large differences at the edges of some inserts. Undersampling streak artifacts  
 318 are also observed in images from both scanners, and are attributed to the limited number  
 319 of projections (90) used. We confirmed that for the phase-II scanner these vanish when  
 320 360 projections are used (not shown). The  $\text{RSP}_{\text{acc}}$  results are listed in table 2-phase-II and  
 321 table 3-pVDA.

---

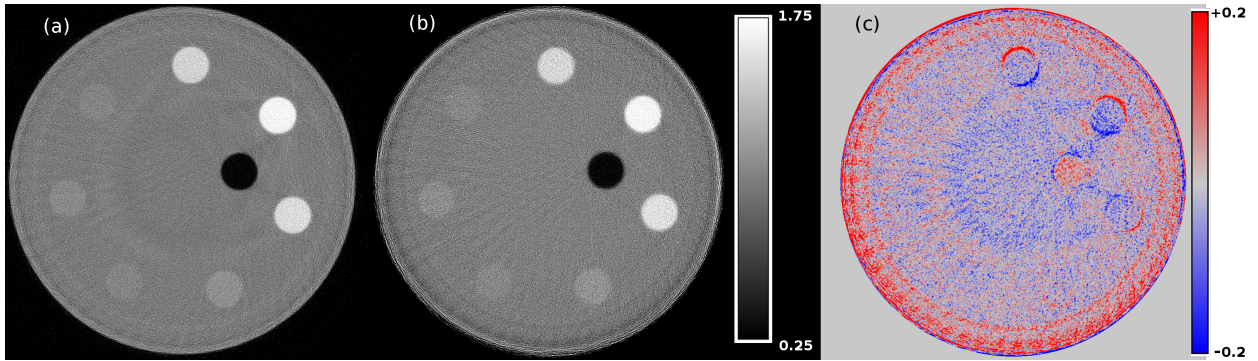


Figure 3: Reconstructed RSP images with  $0.2 \text{ mm} \times 0.2 \text{ mm}$  pixel size from (a) the phase-II and (b) the pVDA scanner. The average of 20 central slices was taken to reduce noise and the images are shown with an RSP level of 1.0 and window of 1.5. In (c) the difference (b)–(a) is shown with an RSP level of 0 and window of 0.4.

322 In the case of the phase-II scanner (table 2), the  $\text{RSP}_{\text{acc}}$  varied from  $-0.29\%$  for the  
 323 brain insert up to  $-4.5\%$  for the sinus. Except for the sinus, the enamel insert ( $-1.03\%$ ) and  
 324 the phantom body ( $-1.33\%$ ), the  $\text{RSP}_{\text{acc}}$  was better than  $1\%$ . The MAPE over all inserts  
 325 and the phantom body for the phase-II scanner image was  $1.14\%$ . Excluding the phantom  
 326 body, the MAPE marginally improved to  $1.12\%$ . Excluding the sinus, the MAPE reached  
 327  $0.72\%$ . Finally, excluding both the sinus and the body of the phantom from the  $\text{RSP}_{\text{acc}}$   
 328 quantification, yielded a MAPE of  $0.63\%$ .

Table 2: Results of the RSP analysis for the phase-II scanner data. The table lists for each insert the  $\text{RSP}_{\text{ref}}$ , the  $\text{RSP}_{\text{mean}}$ , the  $\text{RSP}_{\text{acc}}$  and the size of the ROI in voxels. For different subsets of inserts, the MAPE is also listed. The uncertainty on each value was obtained as explained in section II.H..

Insert	$\text{RSP}_{\text{ref}}$	$\text{RSP}_{\text{mean}}$	$\text{RSP}_{\text{acc}} / \%$	ROI size / voxels
Cortical bone	$1.555 \pm 0.004$	$1.543 \pm 0.0006$	$-0.77 \pm 0.25$	3120
Trabecular bone	$1.100 \pm 0.003$	$1.095 \pm 0.0006$	$-0.45 \pm 0.25$	3060
Spinal disc	$1.070 \pm 0.003$	$1.066 \pm 0.0005$	$-0.37 \pm 0.25$	3080
Enamel	$1.755 \pm 0.004$	$1.737 \pm 0.0005$	$-1.03 \pm 0.25$	3060
Dentin	$1.495 \pm 0.004$	$1.481 \pm 0.0006$	$-0.94 \pm 0.25$	3020
Sinus	$0.200 \pm 0.005$	$0.191 \pm 0.0005$	$-4.50 \pm 0.35$	3040
Phantom body	$0.980 \pm 0.002$	$0.967 \pm 0.0001$	$-1.33 \pm 0.25$	46100
Spinal cord	$1.040 \pm 0.003$	$1.034 \pm 0.0005$	$-0.58 \pm 0.25$	3060
Brain	$1.040 \pm 0.003$	$1.037 \pm 0.0005$	$-0.29 \pm 0.25$	3100
MAPE (all values)			$1.14 \pm 0.09$	
MAPE (w/o body)			$1.12 \pm 0.09$	
MAPE (w/o sinus)			$0.72 \pm 0.09$	
MAPE (w/o body and sinus)			$0.63 \pm 0.10$	

329 For the pVDA scanner (table 3), the  $RSP_{acc}$  varied from 0.1% for the spinal cord and  
 330 brain inserts up to  $-2.4\%$  for the phantom body. Except for the body of the phantom, the  
 331 only other insert for which the  $RSP_{acc}$  was worse than 1% was the sinus with  $-1.5\%$ . The  
 332 MAPE over all inserts and the phantom body was 0.81%. When excluding the phantom  
 333 body, the MAPE improved to 0.61%. Excluding the sinus, the MAPE reached 0.72%. When  
 334 excluding both the sinus and the body of the phantom, the MAPE became 0.48%. The  
 335  $RSP_{acc}$  per insert and the MAPE are displayed in figure 4 for both scanners.

Table 3: Results of the RSP analysis for the pVDA scanner data. The table lists for each insert the  $RSP_{ref}$ , the  $RSP_{mean}$ , the  $RSP_{acc}$  and the size of the ROI in voxels. For different subsets of inserts, the MAPE is also listed. The uncertainty on each value was obtained as explained in section II.H..

Insert	$RSP_{ref}$	$RSP_{mean}$	$RSP_{acc} / \%$	ROI size / voxels
Cortical bone	$1.555 \pm 0.004$	$1.569 \pm 0.001$	$0.90 \pm 0.26$	3060
Trabecular bone	$1.100 \pm 0.003$	$1.103 \pm 0.001$	$0.27 \pm 0.27$	3100
Spinal disc	$1.070 \pm 0.003$	$1.073 \pm 0.001$	$0.28 \pm 0.28$	3100
Enamel	$1.755 \pm 0.004$	$1.771 \pm 0.001$	$0.91 \pm 0.26$	3120
Dentin	$1.495 \pm 0.004$	$1.507 \pm 0.001$	$0.80 \pm 0.27$	3120
Sinus	$0.200 \pm 0.005$	$0.197 \pm 0.001$	$-1.50 \pm 0.65$	3120
Phantom body	$0.980 \pm 0.002$	$0.957 \pm 0.001$	$-2.40 \pm 0.29$	448860
Spinal cord	$1.040 \pm 0.003$	$1.041 \pm 0.001$	$0.10 \pm 0.28$	3060
Brain	$1.040 \pm 0.003$	$1.041 \pm 0.001$	$0.10 \pm 0.28$	3080
MAPE (all values)			$0.81 \pm 0.11$	
MAPE (w/o body)			$0.61 \pm 0.12$	
MAPE (w/o sinus)			$0.72 \pm 0.10$	
MAPE (w/o body and sinus)			$0.48 \pm 0.10$	

336 The spatial resolution as estimated by the radial edge profile of the three higher RSP  
 337 inserts –enamel, cortical bone and dentin– for both scanners is reported in table 4. The  
 338 phase-II scanner yields a spatial resolution of 0.59 – 0.62 lp/mm, while the analysis for the  
 339 pVDA scanner resulted in a slightly lower spatial resolution of 0.44 – 0.48 lp/mm.

Table 4:  $f_{MTF_{10}}$  results for the three highest RSP inserts of the phase-II and pVDA scanners. The values and their uncertainties in brackets were obtained as described in section II.H.

insert	$f_{MTF_{10}}^{phase-II}$	$f_{MTF_{10}}^{pVDA}$
	(lp/mm)	
Cortical bone	0.61 (0.02)	0.47 (0.02)
Dentin	0.62 (0.02)	0.44 (0.02)
Enamel	0.59 (0.01)	0.48 (0.02)
Mean	0.61 (0.01)	0.46 (0.01)

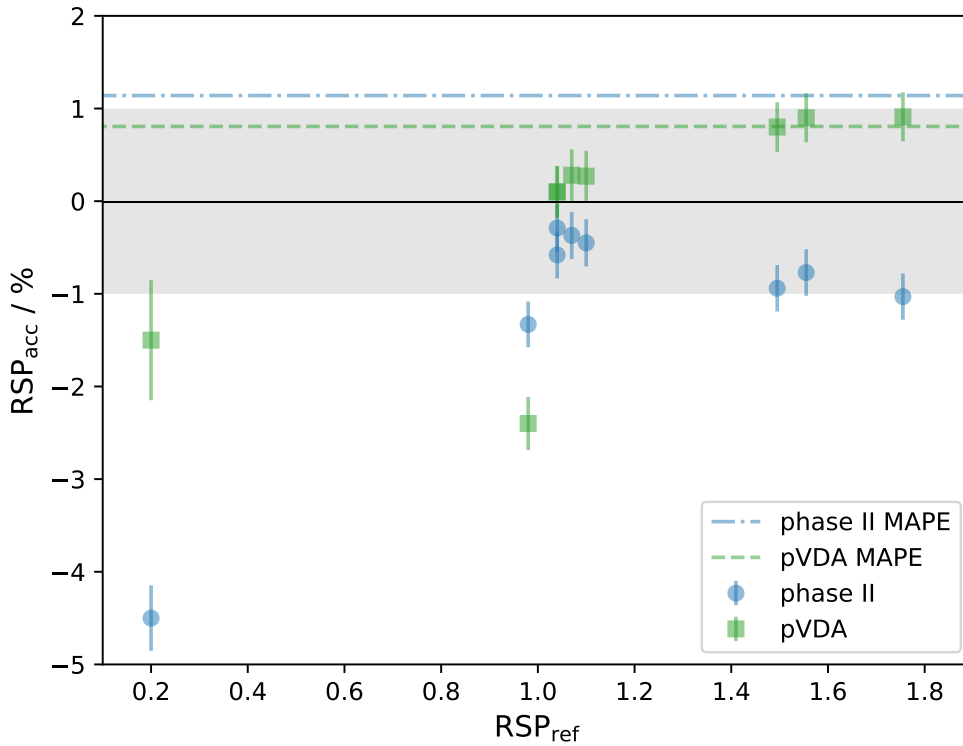


Figure 4: RSP accuracy comparison between the phase-II and the pVDA scanners. Each point represents a  $RSP_{acc}$  value in % from table 2 and table 3, with the corresponding uncertainty depicted as the error bar. The shaded area signifies the  $\pm 1\%$  accuracy range. The dashed and the dotted-dashed lines indicate the MAPE for each scanner, when accounting for all inserts and the body of the phantom.

## 340 IV. Discussion

341 The scope of this study was to compare, in terms of  $RSP_{acc}$  and spatial resolution, two pCT  
 342 scanners of different design available for testing in the same clinical facility. The data were  
 343 collected for the same object on different days, albeit using different proton beam delivery  
 344 methods for the two scanners, namely a wobbled beam for the phase-II scanner and a pencil  
 345 beam for the pVDA scanner.

346 No direct imaging dose estimation was possible, which prevented a comparison of the  
 347 two scanners in terms of RSP noise. This limitation was due to lack of information on the  
 348 total number of protons delivered by the beamline, which has to be operated in low-fluence  
 349 mode for both scanners. The fluence is below the threshold where beam diagnostics function



350 well. The number of protons registered by each scanner correlates to dose, but does not  
351 reflect lost protons due to nuclear interactions, pile up, or other detector inefficiencies.

352 As it may be noticed in figure 3, the pVDA image appears noisier. This is also confirmed  
353 by the  $RSP_{\text{mean}}$  uncertainty per insert shown in table 2 and table 3 (a factor of 1.7–2 higher  
354 for the pVDA scanner), and can be only partially explained by the higher mean proton  
355 fluence in the case of the phase-II scanner. Nevertheless, several effects would have to be  
356 considered before drawing conclusions about a fluence-based noise comparison. One is the  
357 different detector design that could lead to different WEPL or detected energy resolution.  
358 This implies that, even for the same mean fluence, different noise levels could be expected for  
359 each scanner. Another important aspect is that the pVDA image is composed of scans with  
360 three different energies (in general, the lower the energy the higher the energy straggling into  
361 the object). This would have to be considered in any estimation of the noise, and the noise  
362 in the pVDA three-energy image might even have a different spatial distribution compared  
363 to a pVDA single-energy image. Thus, with the data at our disposal, a comparison based  
364 only on the mean fluence would be inconclusive and the topic certainly deserves a separate  
365 investigation.

366 By design, the pVDA scanner cannot use a single proton energy to cover the WEPL  
367 dynamic range required for large objects. Therefore, three different scan energies (118 MeV,  
368 160 MeV and 187 MeV) were used and assembled into a single dataset. It was observed  
369 that the overlap of the two higher energies resulted in strong ring artifacts present in the  
370 RSP image. The optimal RSP image from this dataset was obtained by removing the  
371 overlap between the two highest energies and keeping only the WEPLs sampled from the  
372 160 MeV beam in the region between 100 – 160 mm. The origin of the problematic overlap  
373 between the two higher energies remains unclear, and the solution adopted in this manuscript  
374 might be applicable and valid for this particular dataset only. In a recent work published  
375 by DeJongh,<sup>55</sup> images of the same phantom reconstructed with an iterative reconstruction  
376 algorithm show only very faint RSP artifacts, but a more conclusive investigation would  
377 require comparison of the two algorithms and quantification of the RSP artifacts versus  
378 spatial resolution, especially in the case of high values of the relaxation parameter  $\lambda$ .

379 For the phase-II scanner, the overall MAPE was slightly above 1% ( $1.14 \pm 0.09\%$ ), while  
380 for the pVDA scanner, it was  $0.81 \pm 0.11\%$ . The quantified  $RSP_{\text{acc}}$  of the phase-II scanner

---

381 was strongly affected by the very large relative error of the sinus insert ( $-4.50 \pm 0.35\%$ ).  
382 For the pVDA scanner, the  $RSP_{acc}$  of that insert was also the worst among all inserts  
383 ( $-1.5 \pm 0.65\%$ ), but still closer to the desired  $\pm 1\%$ . When excluding the sinus insert from  
384 the analysis, the MAPE for both scanners was 0.72%. It is worth noting that the absolute  
385 RSP error  $|RSP_{mean} - RSP_{ref}|$  on the sinus insert is not generally higher than that of other  
386 inserts. For the phase-II scanner, the sinus absolute RSP error is 0.009 while the average  
387 absolute RSP error of all inserts is also 0.009 and ranging from 0.003 to 0.018. Similarly, for  
388 the pVDA scanner, the sinus absolute RSP error is 0.003 while the average absolute RSP  
389 error of all inserts is 0.008 and ranging from 0.001 to 0.023. Furthermore, protons traversing  
390 the sinus insert do not have significantly different WEPL compared to protons crossing  
391 other inserts, as the majority of the proton path is traveled across the body of the phantom.  
392 Therefore, the WEPL measurement error of protons traversing the sinus insert and other  
393 inserts is comparable. Thus, the very large relative error of the sinus insert is caused by  
394 its small reference RSP, which is the mean value of the air and the trabecular material of  
395 the sinus composite. It is conceivable that the systematically lower RSP values measured  
396 by both scanners in the case of the sinus insert, are since the mean distance travelled in  
397 the air component is larger than that travelled in the denser material due to preferentially  
398 larger scattering out of the denser material. The next worse  $RSP_{acc}$  for both scanners was  
399 found to be that of the phantom body, with  $-1.33 \pm 0.25\%$  and  $-2.40 \pm 0.29\%$ , respectively.  
400 This is to some extent expected as, unlike the small ROIs used for the inserts, the large  
401 area in which the body of the phantom  $RSP_{acc}$  was quantified contains most of the observed  
402 ring artifacts. For example, quantifying the phantom body RSP in a ROI as large as for  
403 the insert at the center of the phantom yielded an accuracy of  $-0.1\%$  and  $1.63\%$  for the  
404 phase-II and the pVDA scanners, respectively. When the same sized ROI was moved to a  
405 radial distance similar to that of the other inserts, the  $RSP_{acc}$  was  $-0.92\%$  and  $-0.1\%$  for  
406 the phase-II and the pVDA scanners, respectively. Removing the body of the phantom from  
407 the MAPE analysis improves the phase-II scanner accuracy only marginally, from 1.14% to  
408 1.12%, again because it is dominated by the difference in the sinus insert. On the other hand,  
409 for the pVDA the MAPE without the phantom body improves from 0.81% to 0.61%. Finally,  
410 a more selective RSP quantification which excludes both the phantom body and the sinus  
411 yields for both scanners equivalent MAPE of  $0.63 \pm 0.10\%$  and  $0.48 \pm 0.10\%$ . That MAPE of  
412 the phase-II scanner (without sinus and phantom body) agrees well with the result from<sup>41</sup>

---

413 (0.55%), which was obtained from a set of inserts from a different phantom, but covering a  
414 similar RSP range and making use of the same reconstruction algorithm.<sup>29</sup>

415 For both scanners, the spatial resolution obtained from this phantom was within the  
416 range expected for pCT systems. For the phase-II scanner, it varied from 0.59 lp/mm to  
417 0.62 lp/mm. This result is in good agreement with what was reported by Plautz et al.,<sup>56</sup>. In  
418 that work, two quantities where the spatial resolution was quantified, were used to define the  
419 location in a phantom. These were the circle's minimum chord intersecting the insert and  
420 the smallest distance of the insert from the surface of the phantom. For the phantom used in  
421 our study, these values were 130–150 mm in WEPL and about 20–30 mm, respectively. For  
422 the pVDA scanner, the spatial resolution was found to be lower, ranging from 0.44 lp/mm to  
423 0.48 lp/mm. This can be explained by the fact that the phase-II scanner implements a full  
424 tracking capability at the cost of a less compact detector scheme, while the pVDA scanner  
425 comprises a more compact tracker design for future clinical use. Furthermore, the lower  
426 energies used with the pVDA scanner also affect the scattering power of protons, which is  
427 expected to impact spatial resolution.

428 To test this hypothesis, we made use of the formalism published in Krah et al.<sup>54</sup> to  
429 estimate the relative loss of resolution expected from removing downstream position mea-  
430 surements for the phase-II scanner. This led to a decrease of resolution by a factor 1.5,  
431 which is in reasonable agreement with the decrease by a factor 1.2 to 1.4 observed for the  
432 inserts of table 4. It is thus likely that the use of position-only trackers downstream, where  
433 directions cannot be approximated by the vector from the source to the position registered  
434 by the tracker (as opposed to the upstream tracker), contributes chiefly to the lower spatial  
435 resolution of the pVDA scanner. Approximating the pVDA scanner by the phase-II scan-  
436 ner without downstream directions should be valid since both scanners have a distance of  
437 approximately 16 cm between trackers and the isocenter.

438 Whether the difference in spatial resolution affects dosimetric and range prediction  
439 accuracy when pCT is used for treatment planning remains to be investigated. Finally, the  
440 spatial resolution was evaluated at inserts located at relatively large radii. For more central  
441 inserts, where MCS has an increased role, the difference between the two scanners may be  
442 reduced and dominated by the accuracy of the MLP.

---

## 443 V. Conclusion

444 The comparison of the phase-II and pVDA particle tracking pCT scanners showed that they  
445 provide similar  $RSP_{acc}$  (both a MAPE of 0.72%) when excluding the porous sinus insert;  
446 when including it the phase-II scanner performed slightly worse than the pVDA (1.14% vs.  
447 0.81% respectively). Spatial resolution estimated by three high density cylindrical inserts was  
448 found to be 0.61 lp/mm for the phase-II scanner and slightly lower, at 0.46 lp/mm, for the  
449 pVDA scanner. Their spatial resolution performance reflects the different hardware design  
450 choices, with the more compact pVDA tracker, which does not provide directions, leading  
451 to a slightly lower spatial resolution. The clinical significance of these findings remains to  
452 be studied.

## 453 Acknowledgments

454 This work was supported by the Bavaria–California Technology Center (BaCaTeC) project  
455 A1[2018-2], the German Research Foundation (DFG) project #388731804 “Fluence modu-  
456 lated proton computed tomography: a new approach for low–dose image guidance in parti-  
457 cle therapy” and the DFG’s Cluster of Excellence Munich–Centre for Advanced Photonics  
458 (MAP). The authors are thankful to Blake Schultze for proof–reading this manuscript.

## 459 Conflicts of interest

460 M. Pankuch and R. W. Schulte are members of the advisory board of ProtonVDA LLC. E.  
461 DeJongh is employed by ProtonVDA LLC.

## 462 References

- 463
- 464 <sup>1</sup> H. Paganetti, Range uncertainties in proton therapy and the role of Monte Carlo simu-  
465 lations., *Physics in Medicine and Biology* **57**, R99–117 (2012).
  - 466 <sup>2</sup> U. Schneider, E. Pedroni, and A. Lomax, The calibration of CT Hounsfield units for  
467 radiotherapy treatment planning., *Physics in Medicine and Biology* **41**, 111–124 (1996).
-

- 
- 468 <sup>3</sup> M. Yang, X. R. Zhu, P. C. Park, U. Titt, R. Mohan, G. Virshup, J. E. Clayton,  
469 and L. Dong, Comprehensive analysis of proton range uncertainties related to pa-  
470 tient stopping-power-ratio estimation using the stoichiometric calibration., *Physics in*  
471 *Medicine and Biology* **57**, 4095–4115 (2012).
- 472 <sup>4</sup> G. Landry and C.-H. Hua, Current state and future applications of radiological image  
473 guidance for particle therapy., *Medical Physics* **45**, e1086–e1095 (2018).
- 474 <sup>5</sup> N. Hünemohr, B. Krauss, C. Tremmel, B. Ackermann, O. Jäkel, and S. Greulich, Exper-  
475 imental verification of ion stopping power prediction from dual energy CT data in tissue  
476 surrogates, *Physics in Medicine and Biology* **59**, 83 (2013a).
- 477 <sup>6</sup> A. E. Bourque, J.-F. Carrier, and H. Bouchard, A stoichiometric calibration method  
478 for dual energy computed tomography., *Physics in Medicine and Biology* **59**, 2059–2088  
479 (2014).
- 480 <sup>7</sup> N. Hudobivnik, F. Schwarz, T. Johnson, L. Agolli, G. Dedes, T. Tessonier, F. Verhae-  
481 gen, C. Thieke, C. Belka, W. H. Sommer, K. Parodi, and G. Landry, Comparison of  
482 proton therapy treatment planning for head tumors with a pencil beam algorithm on  
483 dual and single energy CT images., *Medical Physics* **43**, 495 (2016).
- 484 <sup>8</sup> C. Möhler, P. Wohlfahrt, C. Richter, and S. Greulich, Range prediction for tissue mixtures  
485 based on dual-energy CT, *Physics in Medicine and Biology* **61**, N268 (2016).
- 486 <sup>9</sup> D. Han, J. V. Siebers, and J. F. Williamson, A linear, separable two-parameter model  
487 for dual energy CT imaging of proton stopping power computation., *Medical Physics*  
488 **43**, 600 (2016).
- 489 <sup>10</sup> V. T. Taasti, J. B. B. Petersen, L. P. Muren, J. Thygesen, and D. C. Hansen, A robust  
490 empirical parametrization of proton stopping power using dual energy CT., *Medical*  
491 *Physics* **43**, 5547 (2016).
- 492 <sup>11</sup> A. Lalonde, E. Bär, and H. Bouchard, A Bayesian approach to solve proton stopping  
493 powers from noisy multi-energy CT data, *Medical Physics* **44**, 5293–5302 (2017).
- 494 <sup>12</sup> M. Saito and S. Sagara, Simplified derivation of stopping power ratio in the human body  
495 from dual-energy CT data., *Medical Physics* **44**, 4179–4187 (2017).
-

- 496 <sup>13</sup> I. P. Almeida, L. E. J. R. Schyns, A. Vaniqui, B. van der Heyden, G. Dedes, A. F.  
497 Resch, F. Kamp, J. D. Zindler, K. Parodi, G. Landry, and F. Verhaegen, Monte Carlo  
498 proton dose calculations using a radiotherapy specific dual-energy CT scanner for tissue  
499 segmentation and range assessment., *Physics in Medicine and Biology* **63**, 115008 (2018).
- 500 <sup>14</sup> G. Landry, F. Dörringer, S. Si-Mohamed, P. Douek, J. F. P. J. Abascal, F. Peyrin,  
501 I. P. Almeida, F. Verhaegen, I. Rinaldi, K. Parodi, and S. Rit, Technical Note: Relative  
502 proton stopping power estimation from virtual monoenergetic images reconstructed from  
503 dual-layer computed tomography, *Medical Physics* **46**, 1821–1828 (2019).
- 504 <sup>15</sup> V. T. Taasti, G. J. Michalak, D. C. Hansen, A. J. Deisher, J. J. Kruse, B. Krauss,  
505 L. P. Muren, J. B. B. Petersen, and C. H. McCollough, Validation of proton stopping  
506 power ratio estimation based on dual energy CT using fresh tissue samples., *Physics in  
507 Medicine and Biology* **63**, 015012 (2017).
- 508 <sup>16</sup> E. Bär, A. Lalonde, R. Zhang, K.-W. Jee, K. Yang, G. Sharp, B. Liu, G. Royle,  
509 H. Bouchard, and H.-M. Lu, Experimental validation of two dual-energy CT meth-  
510 ods for proton therapy using heterogeneous tissue samples., *Medical Physics* **45**, 48–59  
511 (2018).
- 512 <sup>17</sup> Y. Xie, C. Ainsley, L. Yin, W. Zou, J. McDonough, T. D. Solberg, A. Lin, and B.-K. K.  
513 Teo, Ex vivo validation of a stoichiometric dual energy CT proton stopping power ratio  
514 calibration., *Physics in Medicine and Biology* **63**, 055016 (2018).
- 515 <sup>18</sup> C. Möhler, T. Russ, P. Wohlfahrt, A. Elter, A. Runz, C. Richter, and S. Greulich, Exper-  
516 imental verification of stopping-power prediction from single- and dual-energy computed  
517 tomography in biological tissues., *Physics in Medicine and Biology* **63**, 025001 (2018).
- 518 <sup>19</sup> K. B. Niepel, M. Stanislawski, M. Wuerl, F. Doerringer, M. Pinto, O. Dietrich, B. Ertl-  
519 Wagner, A. Lalonde, H. Bouchard, E. Pappas, I. Yohannes, M. Hillbrand, G. Landry,  
520 and K. Parodi, Animal tissue-based quantitative comparison of dual-energy CT to SPR  
521 conversion methods using high-resolution gel dosimetry, *Physics in Medicine & Biology*  
522 **66**, 075009 (2021).
- 523 <sup>20</sup> P. Wohlfahrt, C. Möhler, K. Stützer, S. Greulich, and C. Richter, Dual-energy CT based
-

- 524 proton range prediction in head and pelvic tumor patients, *Radiotherapy and Oncology*  
525 **125**, 526–533 (2017b).
- 526 <sup>21</sup> P. Wohlfahrt, C. Möhler, V. Hietschold, S. Menkel, S. Greilich, M. Krause, M. Bau-  
527 mann, W. Enghardt, and C. Richter, Clinical implementation of dual-energy CT for  
528 proton treatment planning on pseudo-monoenergetic CT scans, *International Journal of*  
529 *Radiation Oncology, Biology, Physics* **97**, 427–434 (2017a).
- 530 <sup>22</sup> P. Wohlfahrt, C. Möhler, W. Enghardt, M. Krause, D. Kunath, S. Menkel, E. G. C.  
531 Troost, S. Greilich, and C. Richter, Refinement of the Hounsfield look-up table by  
532 retrospective application of patient-specific direct proton stopping-power prediction from  
533 dual-energy CT, *Medical Physics* **47**, 1796–1806 (2020).
- 534 <sup>23</sup> J. Berthold, C. Khamfongkhrua, J. Petzoldt, J. Thiele, T. Hölscher, P. Wohlfahrt,  
535 N. Peters, A. Jost, C. Hofmann, G. Janssens, J. Smeets, and C. Richter, First-in-human  
536 validation of CT-based proton range prediction using prompt gamma imaging in prostate  
537 cancer treatments, *International Journal of Radiation Oncology Biology Physics* **111**,  
538 1033–1043 (2021).
- 539 <sup>24</sup> P. Zygmanski, K. P. Gall, M. S. Z. Rabin, and S. J. Rosenthal, The measurement  
540 of proton stopping power using proton-cone-beam computed tomography, *Physics in*  
541 *Medicine and Biology* **45**, 511–528 (2000).
- 542 <sup>25</sup> R. W. Schulte, S. N. Penfold, J. T. Tafas, and K. E. Schubert, A maximum likelihood  
543 proton path formalism for application in proton computed tomography., *Medical Physics*  
544 **35**, 4849–4856 (2008).
- 545 <sup>26</sup> S. N. Penfold, A. B. Rosenfeld, R. W. Schulte, and K. E. Schubert, A more accurate  
546 reconstruction system matrix for quantitative proton computed tomography., *Medical*  
547 *Physics* **36**, 4511–4518 (2009).
- 548 <sup>27</sup> S. N. Penfold, R. W. Schulte, Y. Censor, and A. B. Rosenfeld, Total variation superior-  
549 ization schemes in proton computed tomography image reconstruction., *Medical Physics*  
550 **37**, 5887–5895 (2010).
- 551 <sup>28</sup> D. C. Hansen, N. Bassler, T. S. Sørensen, and J. Seco, The image quality of ion computed  
552 tomography at clinical imaging dose levels, *Medical Physics* **41**, 111908 (2014).
-

- 553 <sup>29</sup> S. Rit, G. Dedes, N. Freud, D. Sarrut, and J. M. Létang, Filtered backprojection proton  
554 CT reconstruction along most likely paths., *Medical Physics* **40**, 031103 (2013).
- 555 <sup>30</sup> G. Poludniowski, N. M. Allinson, and P. M. Evans, Proton computed tomography  
556 reconstruction using a backprojection-then-filtering approach., *Physics in Medicine and*  
557 *Biology* **59**, 7905–7918 (2014).
- 558 <sup>31</sup> F. Khellaf, N. Krah, J. M. Létang, C.-A. Collins-Fekete, and S. Rit, A comparison of  
559 direct reconstruction algorithms in proton computed tomography, *Physics in Medicine*  
560 *& Biology* **65**, 105010 (2020a).
- 561 <sup>32</sup> Y. Takada, K. Kondo, T. Marume, K. Nagayoshi, I. Okada, and K. Takikawa, Proton  
562 computed tomography with a 250 MeV pulsed beam, *Nucl. Instr. Meth. Phys. Res. A*  
563 **273**, 410–422 (1988).
- 564 <sup>33</sup> G. Coutrakon, V. Bashkirov, F. Hurley, R. Johnson, V. Rykalin, H. Sadrozinski, and  
565 R. Schulte, Design and construction of the 1st proton CT scanner, in *AIP Conference*  
566 *Proceedings 1525*, 327 (2013), 2013.
- 567 <sup>34</sup> H. F.-W. Sadrozinski, T. Geoghegan, E. Harvey, R. P. Johnson, T. E. Plautz, A. Zat-  
568 serklyaniy, V. Bashkirov, R. F. Hurley, P. Piersimoni, R. W. Schulte, P. Karbasi, K. E.  
569 Schubert, B. Schultze, and V. Giacometti, Operation of the Preclinical Head Scanner  
570 for Proton CT., *Nucl. Instr. Meth. Phys. Res. A* **831**, 394–399 (2016).
- 571 <sup>35</sup> R. P. Johnson, V. Bashkirov, L. DeWitt, V. Giacometti, R. F. Hurley, P. Piersimoni,  
572 T. E. Plautz, H. F.-. Sadrozinski, K. Schubert, R. Schulte, B. Schultze, and A. Zat-  
573 serklyaniy, A Fast Experimental Scanner for Proton CT: Technical Performance and  
574 First Experience With Phantom Scans, *IEEE Transactions on Nuclear Science* **63**, 52–  
575 60 (2016).
- 576 <sup>36</sup> H. E. S. Pettersen, J. Alme, A. Biegun, A. van den Brink, M. Char, D. Fehlker, I. Meric,  
577 O. H. Odland, T. Peitzmann, E. Rocco, H. Wang, S. Yang, C. Zhang, and D. Röhrich,  
578 Proton tracking in a high-granularity Digital Tracking Calorimeter for proton CT pur-  
579 poses, *Nucl. Instr. Meth. Phys. Res. A* 860 51-61 (2016).
- 580 <sup>37</sup> M. Esposito, C. Waltham, J. T. Taylor, S. Manger, B. Phoenix, T. Price, G. Polud-  
581 niowski, S. Green, P. M. Evans, P. P. Allport, S. Manolopoulos, J. Nieto-Camero,
-



- 582 J. Symons, and N. M. Allinson, PRaVDA: The first solid-state system for proton com-  
583 puted tomography., *Physica Medica* **55**, 149–154 (2018).
- 584 <sup>38</sup> C. Civinini, M. Scaringella, M. Brianzi, M. Intravaia, N. Randazzo, V. Sipala, M. Rovi-  
585 tuso, F. Tommasino, M. Schwarz, and M. Bruzzi, Relative stopping power measure-  
586 ments and prosthesis artifacts reduction in proton CT, *Physics in Medicine & Biology*  
587 **65**, 225012 (2020).
- 588 <sup>39</sup> D. C. Hansen, T. Sangild Sørensen, and S. Rit, Fast reconstruction of low dose proton  
589 CT by sinogram interpolation., *Physics in Medicine and Biology* **61**, 5868–5882 (2016).
- 590 <sup>40</sup> V. Giacometti, V. A. Bashkirov, P. Piersimoni, S. Guatelli, T. E. Plautz, H. F.-W.  
591 Sadrozinski, R. P. Johnson, A. Zatserklyaniy, T. Tessonnier, K. Parodi, A. B. Rosenfeld,  
592 and R. W. Schulte, Software platform for simulation of a prototype proton CT scanner.,  
593 *Medical Physics* **44**, 1002–1016 (2017a).
- 594 <sup>41</sup> G. Dedes, J. Dickmann, K. Niepel, P. Wesp, R. P. Johnson, M. Pankuch, V. Bashkirov,  
595 S. Rit, L. Volz, R. W. Schulte, G. Landry, and K. Parodi, Experimental comparison of  
596 proton CT and dual energy x-ray CT for relative stopping power estimation in proton  
597 therapy., *Physics in Medicine and Biology* **64**, 165002 (2019).
- 598 <sup>42</sup> C. Sarosiek, E. A. DeJongh, G. Coutrakon, D. F. DeJongh, K. L. Duffin, N. T. Karonis,  
599 C. E. Ordoñez, M. Pankuch, V. Rykalin, J. R. Winans, and J. S. Welsh, Analysis of  
600 characteristics of images acquired with a prototype clinical proton radiography system,  
601 *Medical Physics* (2021).
- 602 <sup>43</sup> E. A. DeJongh, D. F. DeJongh, I. Polnyi, V. Rykalin, C. Sarosiek, G. Coutrakon, K. L.  
603 Duffin, N. T. Karonis, C. E. Ordoñez, M. Pankuch, J. R. Winans, and J. S. Welsh,  
604 Technical Note: A fast and monolithic prototype clinical proton radiography system  
605 optimized for pencil beam scanning, *Medical Physics* **48**, 1356–1364 (2021).
- 606 <sup>44</sup> D. F. DeJongh, E. A. DeJongh, V. Rykalin, G. DeFillippo, M. Pankuch, A. W. Best,  
607 G. Coutrakon, K. L. Duffin, N. T. Karonis, C. E. Ordoñez, C. Sarosiek, R. W. Schulte,  
608 J. R. Winans, A. M. Block, C. L. Hentz, and J. S. Welsh, A comparison of proton  
609 stopping power measured with proton CT and x-ray CT in fresh postmortem porcine  
610 structures, *Medical Physics* (2021).
-

- 611 <sup>45</sup> V. A. Bashkirov, R. W. Schulte, R. F. Hurley, R. P. Johnson, H. F.-W. Sadrozinski,  
612 A. Zatserklyaniy, T. Plautz, and V. Giacometti, Novel scintillation detector design and  
613 performance for proton radiography and computed tomography., *Medical Physics* **43**,  
614 664–674 (2016).
- 615 <sup>46</sup> J. Dickmann, C. Sarosiek, V. Rykalin, M. Pankuch, S. Rit, N. Detrich, G. Coutrakon,  
616 R. P. Johnson, R. W. Schulte, K. Parodi, G. Landry, and G. Dedes, Experimental real-  
617 ization of dynamic fluence field optimization for proton computed tomography, *Physics*  
618 *in Medicine & Biology* **65**, 195001 (2020a).
- 619 <sup>47</sup> A. Artikov, J. Budagov, I. Chirikov-Zorin, D. Chokheli, M. Lyablin, G. Bellettini,  
620 A. Menzione, S. Tokar, N. Giokaris, and A. Manousakis-Katsikakis, Properties of the  
621 Ukraine polystyrene-based plastic scintillator UPS 923A, *Nuclear Instruments Methods*  
622 *in Physics Research, Section A: Accelerators, Spectrometers, Detectors, and Associated*  
623 *Equipment* **555**, 125–131 (2005).
- 624 <sup>48</sup> G. Dedes, R. P. Johnson, M. Pankuch, N. Detrich, W. M. A. Pols, S. Rit, R. W. Schulte,  
625 K. Parodi, and G. Landry, Experimental fluence-modulated proton computed tomogra-  
626 phy by pencil beam scanning., *Medical Physics* **45**, 3287–3296 (2018).
- 627 <sup>49</sup> B. Schultze, P. Karbasi, C. Sarosiek, G. Coutrakon, C. E. Ordonez, N. T. Karonis, K. L.  
628 Duffin, V. A. Bashkirov, R. P. Johnson, K. E. Schubert, and R. W. Schulte, Particle-  
629 Tracking Proton Computed Tomography—Data Acquisition, Preprocessing, and Pre-  
630 conditioning, *IEEE Access* **9**, 25946–25958 (2021).
- 631 <sup>50</sup> P. Piersimoni, J. Ramos-Méndez, T. Geoghegan, V. Bashkirov, R. Schulte, and B. Fadde-  
632 gon, The effect of beam purity and scanner complexity on proton CT accuracy, *Medical*  
633 *Physics* **44**, 284–298 (2017).
- 634 <sup>51</sup> G. Dedes, J. Dickmann, V. Giacometti, S. Rit, N. Krah, S. Meyer, V. Bashkirov,  
635 R. Schulte, R. P. Johnson, K. Parodi, and G. Landry, The role of Monte Carlo simula-  
636 tion in understanding the performance of proton computed tomography, *Zeitschrift für*  
637 *Medizinische Physik* (2020).
- 638 <sup>52</sup> J. Dickmann, C. Sarosiek, V. Rykalin, M. Pankuch, G. Coutrakon, R. P. Johnson,  
639 V. Bashkirov, R. W. Schulte, K. Parodi, G. Landry, and G. Dedes, Proof of concept
-

- 640 image artifact reduction by energy-modulated proton computed tomography (EMpCT),  
641 *Physica Medica* **81**, 237–244 (2021).
- 642 <sup>53</sup> S. Richard, D. B. Husarik, G. Yadava, S. N. Murphy, and E. Samei, Towards task-based  
643 assessment of CT performance: System and object MTF across different reconstruction  
644 algorithms, *Medical Physics* **39**, 4115–4122 (2012).
- 645 <sup>54</sup> N. Krah, F. Khellaf, J. M. Létang, S. Rit, and I. Rinaldi, A comprehensive theoretical  
646 comparison of proton imaging set-ups in terms of spatial resolution, *Physics in Medicine  
647 & Biology* **63**, 135013 (2018).
- 648 <sup>55</sup> D. F. D. Jongh and E. A. D. Jongh, An Iterative Least Squares Method for Proton CT  
649 Image Reconstruction., *IEEE Transactions on Radiation and Plasma Medical Sciences*  
650 , 1–1 (2021).
- 651 <sup>56</sup> T. E. Plautz, V. Bashkirov, V. Giacometti, R. F. Hurley, R. P. Johnson, P. Piersimoni,  
652 H. F.-W. Sadrozinski, R. W. Schulte, and A. Zatserklyaniy, An evaluation of spatial  
653 resolution of a prototype proton CT scanner, *Medical Physics* **43**, 6291–6300 (2016).
-